This is an open access article published under an ACS AuthorChoice License, which permits copying and redistribution of the article or any adaptations for non-commercial purposes.

ACS APPLIED MATERIALS & INTERFACES

ACS AUTHORCHOICE

Research Article

Cite This: ACS Appl. Mater. Interfaces 2018, 10, 12975−12982

www.acsami.org

Stokes-Shift-Engineered Indium Phosphide Quantum Dots for Efficient Luminescent Solar Concentrators

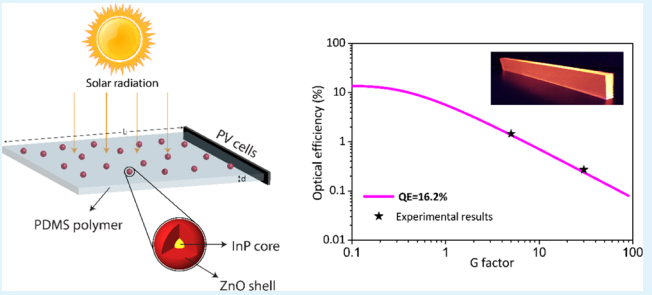
Sadra Sadeghi,[†,⊥] Houman Bahmani Jalali,[‡,⊥] Rustamzhon Melikov,[§] Baskaran Ganesh Kumar,[§] Mohammad Mohammadi Aria,[‡] Cleva W. Ow-Yang,[∥] and Sedat Nizamoglu*[,†,‡,§]

[†]Graduate School of Materials Science and Engineering, [‡]Department of Biomedical Sciences and Engineering, and [§]Department of Electrical and Electronics Engineering, Koç University, Istanbul 34450, Turkey

[∥]Department of Engineering and Natural Sciences, Sabanci University, Istanbul 34956, Turkey

Supporting Information

ABSTRACT: Luminescent solar concentrators (LSCs) show promise because of their potential for low-cost, large-area, and high-efficiency energy harvesting. Stokes shift engineering of luminescent quantum dots (QDs) is a favorable approach to suppress reabsorption losses in LSCs; however, the use of highly toxic heavy metals in QDs constitutes a serious concern for environmental sustainability. Here, we report LSCs based on cadmium-free InP/ZnO core/shell QDs with type-II band alignment that allow for the suppression of reabsorption by Stokes shift engineering. The spectral emission and absorption overlap was controlled by the growth of a ZnO shell on an InP core. At the same time, the ZnO layer also facilitates the photostability of the QDs within the host matrix. We analyzed the optical performance of indium-based LSCs and identified the optical efficiency as 1.45%. The transparency, flexibility, and cadmium-free content of the LSCs hold promise for solar window applications.



KEYWORDS: *Stokes shift, quantum dots, luminescent solar concentrator, reabsorption, type-II, band alignment, solar cell, indium phosphide (InP)*

INTRODUCTION

Today, there exists an intense worldwide effort toward the use of green energy production technologies because of the concerns about environmental sustainability and global warming. Among ecofriendly power technologies (wind, wave, etc.), solar radiation provides a clean and abundant form of energy. To harvest solar energy, silicon-based photovoltaic (Si-PV) cells have received significant attention in the last three decades,[1−4] and recently, the cost of Si-PV modules has lowered down to 70%, which substantially shortened the economic payback period.[5] The improvement in energy efficiency of these PV systems can further enhance their potential for the widespread use. To fulfill this demand, conventional solar concentrators that use mobile mirrors and lenses have been developed to track the sun and improve the sunlight energy harvesting.[6] However, they have some drawbacks, such as costly optomechanical equipment to track the sun, cooling focal point of the mirrors, and inadequacy to concentrate the diffused sunlight.[7]

Luminescent solar concentrators (LSCs) have been explored as a versatile platform to improve the energy production capability of Si-PVs and consequently to reduce the energy production cost per unit watt.[2,8−11] A typical LSC consists of an optical waveguide that includes photoluminescent materials, which absorb direct and diffused sunlight radiation and re-emit at higher wavelengths.[12−15] The downconverted luminescence is then guided by total internal reflection (TIR) and absorbed by the PV cells placed at the edges of the waveguide.[16] As the lateral area of an LSC is significantly larger than its edge area, the generated photon density is considerably increased because of the "concentrator effect", which results in improved energy harvesting.[15] By coordinating the wavelength of the PV responsivity maxima with the photoluminescence (PL) peak wavelength of the fluorescent emitters, the output power can be exceptionally enhanced.[17] Moreover, the transparency of these concentrators makes them suitable to be utilized as "solar windows".[3,17,18]

Among the wide variety of fluorescent materials, colloidal quantum dots (QDs) show advantageous properties such as high PL quantum efficiency (QE), spectral tunability via quantum confinement effect, and high photostability.[1,19−27] Even though the QDs show a high QE after synthesis, their performance in LSC applications is limited because of the reabsorption.[28,29] The reabsorption losses can be decreased by increasing the Stokes shift, which is the energy separation between the emission and absorption spectra. The Stokes shift

Received: December 17, 2017
Accepted: March 28, 2018
Published: March 28, 2018

Downloaded from pubs.acs.org/aamick/article-pdf/10/15/12975/6692023/acsami.7b19144.pdf by KOC UNIV user on 29 October 2026

© 2018 American Chemical Society

DOI: 10.1021/acsami.7b19144
ACS Appl. Mater. Interfaces 2018, 10, 12975−12982

can be controlled by using indirect band gap materials,[30] varying the semiconductor compositions,[31] and doping with transition-metal ions.[7,17,32−34]

Alternatively, heterojunction formation in QDs provides an effective approach to engineer the Stokes shift. The transition from a type-I to a quasi-type-II carrier localization can decrease the spectral emission and absorption overlap.[17] So far, this is typically achieved by the growth of a thick shell on CdSe core QDs.[17] This thick shell also allows for the minimization of the host material effect, which significantly decreases the efficiency drop of the QDs when transferred from the solution into the polymer matrix. Even though this approach is advantageous to simultaneously suppress the reabsorption losses and the host material effect, there are major concerns about the use of the highly toxic cadmium content in various applications.[35,36] Indium phosphide (InP) QD is a strong alternative to cadmium-based QD because of its non-toxic material content.[37−39] Indium has been used in commercial applications in TVs (e.g., InGaN light-emitting diodes), which shows the mass production potential and its safe use.[40,41] Therefore, the development of indium-based QDs with low reabsorption losses and low host-material sensitivity is essential.

In this study, we demonstrated InP/ZnO core/shell QD-based LSCs that show a significant suppression of reabsorption over a long optical path. We performed colloidal synthesis and nanoengineered the InP/ZnO core/shell QDs for efficient solar concentration. The ZnO shell growth on InP core QDs facilitated a type-II band alignment (Figure 1a),[42] which leads to increasing the Stokes shift and decreasing the reabsorption losses. For LSC fabrication, we incorporated the QDs into the polydimethylsiloxane (PDMS) waveguide, and the QE and time-resolved measurements confirmed that the host material effect is also simultaneously reduced.

RESULTS AND DISCUSSION

ZnO was grown on an InP core by the thermal decomposition of zinc acetylacetonate ($Zn(acac)_2$). Previously, zinc acetate ($Zn(OAc)_2$) and $Zn(acac)_2$ have been used as precursors for synthesizing ZnO QDs,[43−47] but $Zn(acac)_2$ resulted in smaller and more monodisperse ZnO QDs with a weaker trap emission.[47] Moreover, using oleylamine (OAM) as the stabilizing agent can help to prevent the ZnO grain from aggregating.[45] To synthesize highly luminescent InP cores, we used zinc undecylenate as the surface passivator[48] and OAM and oleic acid (OA) as the stabilizing ligands. In short, InP cores were synthesized by the hot injection of tris-(trimethylsilyl)phosphine ($P(TMS)_3$) on indium chloride ($InCl_3$) in the presence of the OAM and OA ligands with the 1-octadecene (ODE) solvent. Once the InP core was formed, the ZnO stock solution consisting of $Zn(acac)_2$, OAM, OA, and ODE was added to the InP core solution and heated to 280 °C (see the Methods and Characterization section for the detailed synthesis procedure). Even though the lattice mismatch between InP and ZnO is 11%, which is higher than the well-known InP/ZnS lattice mismatch (~8%),[49] the synthesized InP/ZnO QDs exhibit excellent optical and electronic properties similar to those of the previously reported type-II heterostructure of CdTe/ZnSe with a higher lattice mismatch of up to 14%.[50] The ZnO crystal growth on InP was observed with the increase of the QD diameter from 1.95 nm for the InP-only core to 3.01 nm for InP/2ZnO (with two times shelling) and 4.31 nm for InP/5ZnO (with five times shelling), where each shelling corresponds to a thickness of

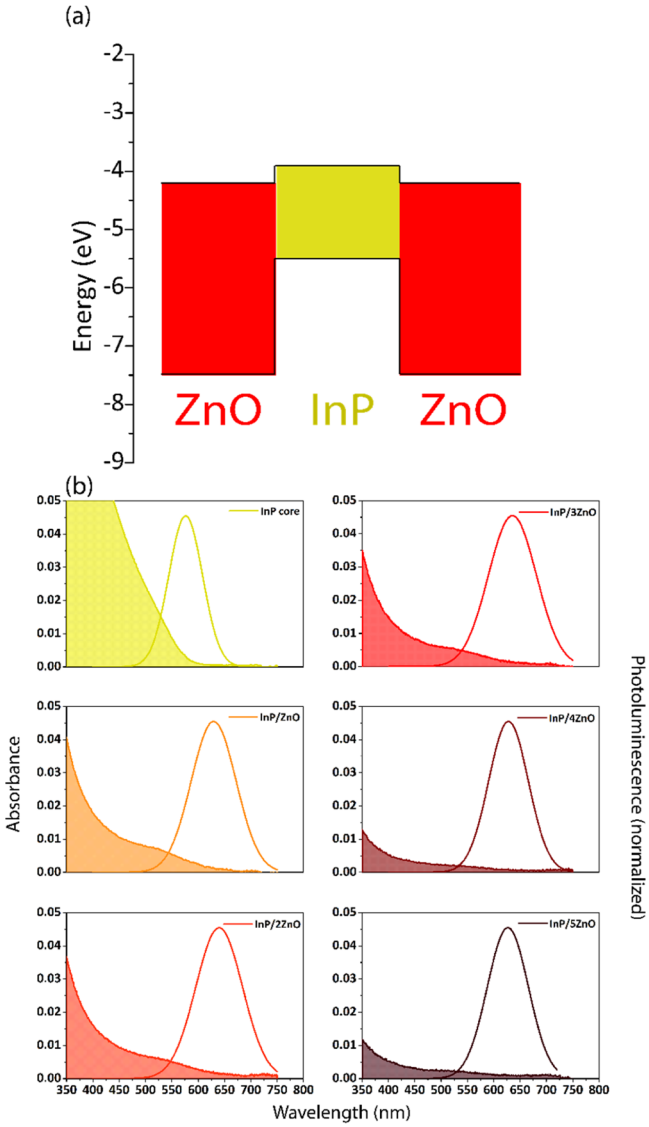


Figure 1. (a) Band alignment of the InP/ZnO core/shell QDs. (b) Absorption (shading) and PL (no shading) spectra of the InP/ZnO QDs with increasing shell layers (from zero to five) in hexane. Each shell layer corresponded to a shell thickness of 0.27 nm.

~0.27 nm (Figure S1). In addition, we carried out scanning electron microscopy−energy-dispersive X-ray spectrometry (SEM−EDXS) measurements (Figure S2a−c), and the InP/ZnO structures showed a progressive enhancement of the zinc content from 10.70 wt % for the InP core structure to 23.33 wt % for the InP/5ZnO core/shell structures (Table S2). Moreover, the synthesized QDs studied by powder X-ray diffraction (PXRD) showed a crystal structure, and InP and ZnO showed a cubic and hexagonal structures, respectively (Figure S3). Additionally, the transmission electron microscopy (TEM) and X-ray diffraction (XRD) measurements confirmed the presence of the InP/ZnO core/shell structure, which caused the significant red shift in the PL peak position.

The absorbance and PL spectra of the synthesized QDs were characterized to investigate the effect of shell thickness on their optical properties (as shown in Figure 1b). The emission peak wavelength of the QDs was red-shifted from 576 to 627 nm by growing a ZnO shell on the InP core because the electron had a tendency to delocalize toward the ZnO shell, while the hole was

Downloaded from pubs.acs.org/aamick/article-pdf/10/15/12975/6692023/acsami.7b19144.pdf by KOC UNIV user on 29 October 2026

DOI: 10.1021/acsami.7b19144
ACS Appl. Mater. Interfaces 2018, 10, 12975−12982

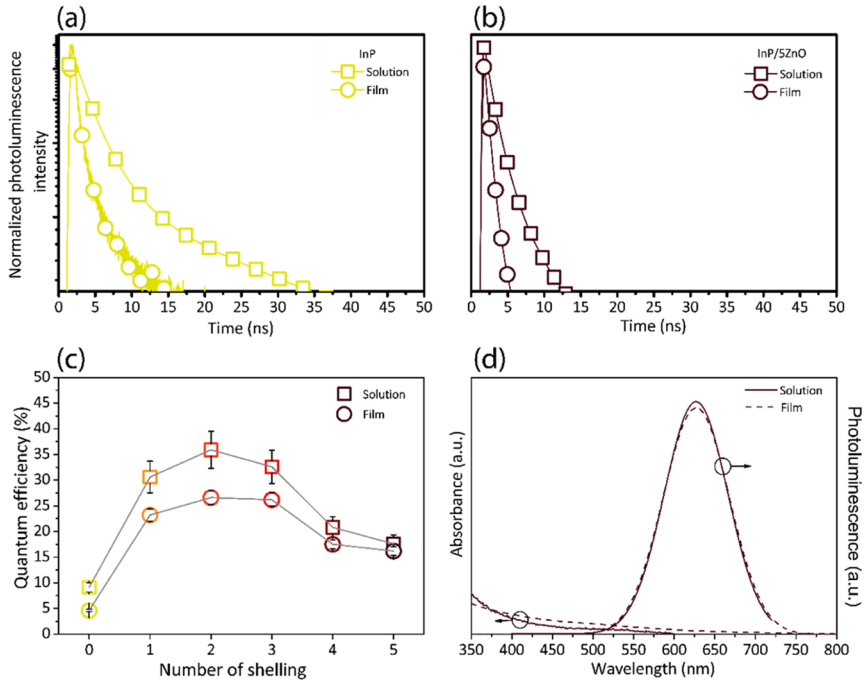


Figure 2. (a,b) Time-resolved fluorescence measurements of InP and InP/5ZnO QDs in hexane (square) and PDMS film (circle). (c) QE of the corresponding QDs in the hexane solution (square) and the PDMS film (circle) (N = 3). (d) Absorption and PL spectra of the InP/5ZnO QDs in the hexane solution (solid line) and in the PDMS film (dashed line).

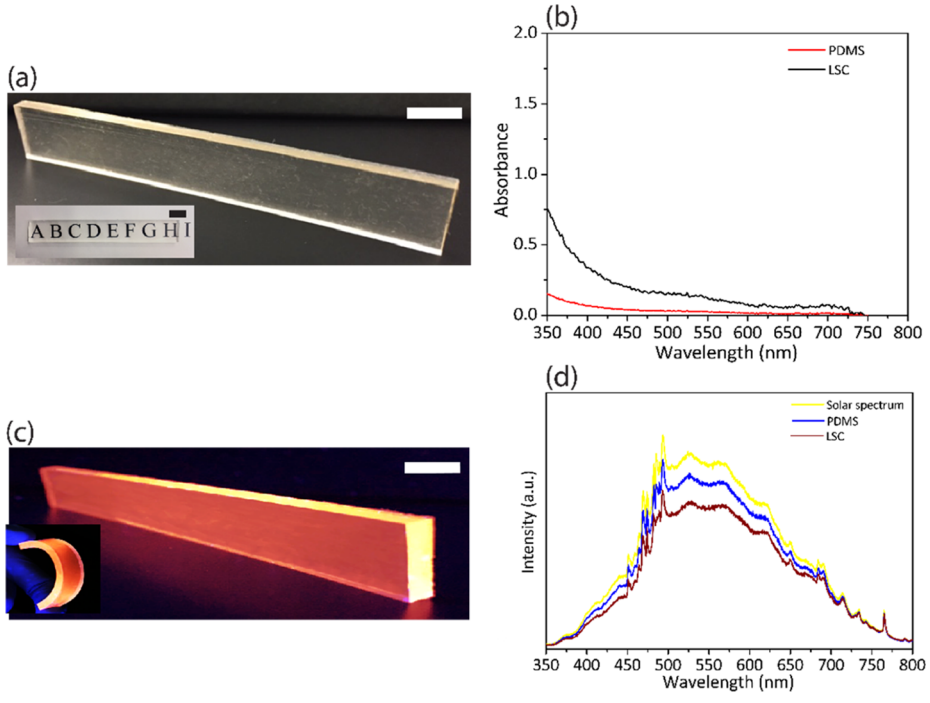


Figure 3. (a) Photograph of InP/5ZnO QD-LSC under ambient light. Inset: frontal view of InP/5ZnO QD-LSC. (b) Absorbance spectra of PDMS and LSC with 0.05 wt % concentration of InP/5ZnO QDs. (c) InP/5ZnO QD-LSC under UV irradiation. The edges seem brighter because of the TIR in LSC. Inset: the flexibility of the QD-LSC. (d) Solar spectrum before and after the PDMS slab and the QD-LSC were incorporated with 0.05 wt % InP/5ZnO QDs. The scale bar is 1 cm in all figures.

strongly confined inside the core (as shown in Figure 1a). Thus, the delocalization of the exciton led to less confinement energy and red shift in the emission. As the shell thickness increased, the electron and hole recombination lifetime also increased from an average value of 11 ns for InP to 31 ns for InP/5ZnO (Figure 2a,b), owing to the smaller cross section of the electron and hole wave function overlap. Noticeably, in Figure 1b, the indium-based type-II heterostructures enabled the control on the Stokes shift, and while the shell thickness increased, the spectral overlap between the emission and absorption significantly decreased (Figure S4). Because the shell volume of the InP/5ZnO QDs was nearly 10 times higher

DOI: 10.1021/acsami.7b19144
ACS Appl. Mater. Interfaces 2018, 10, 12975−12982

Downloaded from pubs.acs.org/aamick/article-pdf/10/15/12975/6692023/acsami.7b19144.pdf by KOC UNIV user on 29 October 2026

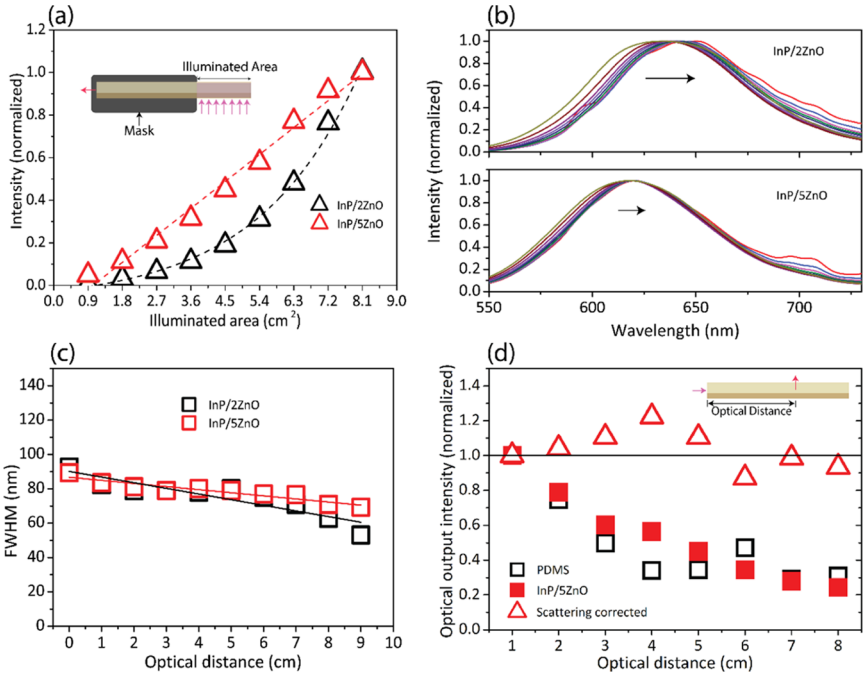


Figure 4. (a) Dependence of the optical output intensity by varying the illuminated area. Both InP/2ZnO (black triangle) and InP/5ZnO (red triangle) QD-LSCs excited at 365 nm UV radiation. Inset: The optical setup configuration in which the illumination was from the bottom and the output light extraction was from the edge. The mask blocks the light and allows for partial illumination. (b) Spectra of the InP/2ZnO (upper panel) and InP/5ZnO (lower panel) QD-LSCs for different optical distances (up to 9 cm). (c) fwhm of the optical output spectra for the InP/2ZnO (black square) and InP/5ZnO (red square) QD-LSCs at different optical distances (the measurements in (b) and (c) were done as shown in the inset of (a)). (d) Optical output intensity of PDMS (black square) and the InP/5ZnO (red filled square) QD-LSC. The scattering-corrected intensity (red triangle) was obtained by subtracting the optical output intensity of PDMS from that of the InP/5ZnO QD-LSC. Inset: The light at 665 nm was coupled from the edge and collected from the top.

than that of the InP core QDs (~300 nm^3 for InP/5ZnO versus only ~30 nm^3 for the InP core), the absorption spectrum was significantly affected by the ZnO shell. This was also observable in their cadmium-based counterparts.[17]

The QE measurements of the QDs in hexane and in the PDMS polymer matrix were performed, as shown in Figure 2c. Increasing the shell thickness up to InP/2ZnO results in a three-fold enhancement in QE (35.9%), which was due to better surface passivation by the shell formation.[51] Further increase of the ZnO shell thickness caused the QE to decrease (i.e., 17.6% for InP/5ZnO) presumably because of the higher interfacial strain, which was generated by an incomplete monolayer (ML) coverage (for a detailed ML coverage calculation, see Table S1).[52] In addition, while the ZnO shell is grown on top of the InP core, the heterostructure shifts from a type-I to a type-II carrier localization, meaning that while the hole is confined in the InP core, the electron localizes in the shell. Up to 2 MLs of ZnO, the QD also possibly shows a quasi-type-II carrier localization, in which both the electron and the hole mainly recombine in the core region. While the shell thickness is further increased, the recombination occurs with an electron that was significantly localized in the shell and a hole in the core, which also leads to a decrease in the oscillator strength and quantum yield.

The QE of the QD slabs (Figure 2c) showed a decrease in comparison with that of the in-solution QDs because of the host material effect, which introduced the additional non-radiative channels. The QE of the films followed a similar trend with the QE of the solutions, which increased up to InP/2ZnO and then decreased as the shell growth continued up to InP/5ZnO. Notably, as the shell thickness increased from two to five layers, the difference between the QE of the films and solutions showed a less change in efficiency. While the QE change was 9.3% for InP/2ZnO, it decreased to 1.4% for InP/5ZnO. This enhanced photostability against the host material effect was also visible in the time-resolved PL decay spectra for the QDs (Figure 2a,b). In both hexane and PDMS, the absorbance of the InP/5ZnO QDs was similar because of the low scattering loss, and the QDs additionally showed a stable PL peak wavelength at 627 nm (Figure 2d). Moreover, we investigated the relative change of the reabsorption loss,[1] and the relative reabsorption decreased while the shell grows (Figure S4).

LSCs should absorb sufficient incident radiation and direct the downconverted luminescence toward the edges for light concentration. For this, 0.05 wt % of QDs was integrated into the PDMS slabs (Figure 3a), and at this loading concentration level, the transparency of LSCs promotes the appropriate reduction of incident sunlight quality that can transmit to the inside of homes and offices (Figure 3a inset). In terms of light harvesting, an LSC absorbs ~24% of the incoming radiation (at 525 nm) (Figure 3b). Moreover, the surfaces of the LSCs were sufficiently smooth for TIR and light guiding. Hence, under UV light exposure, the luminescence of the fabricated slab was especially visible in the edges compared to the faces because of the waveguiding effect (Figure 3c). Furthermore, the flexibility of the QD−polymer slabs is shown in the inset of Figure 3c, and this property can be useful to integrate LSCs on curved surfaces and to keep the light intensity fixed while the sun changes its position during the day.

To evaluate the change in the photometric quality of the light that passes through the LSCs, it was illuminated by a collimated

Downloaded from pubs.acs.org/aamick/article-pdf/10/15/12975/6692023/acsami.7b19144.pdf by KOC UNIV user on 29 October 2026

DOI: 10.1021/acsami.7b19144
ACS Appl. Mater. Interfaces 2018, 10, 12975−12982

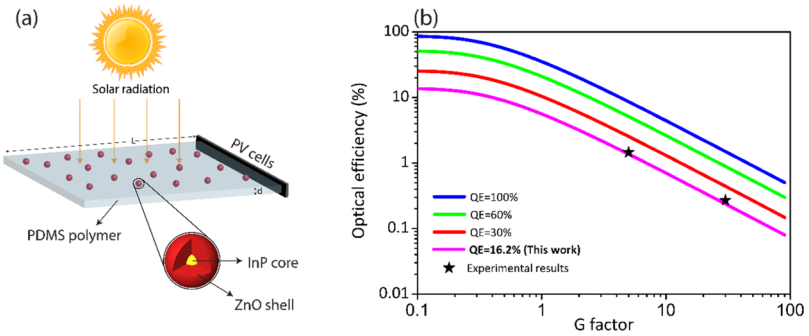


Figure 5. (a) Schematic of an LSC that consists of the InP/ZnO core/shell QDs inside the PDMS polymer matrix. The light at the edge will be absorbed by the photovoltaic cells and converted into electrical power. The geometry of the LSC (L and d) affects the optical efficiency by changing the geometrical factor. (b) Simulations were done for the QE levels of QDs as 16.2, 30, 60, and 100%. The star symbol indicated the experimental measurements of LSCs with a loading concentration of 0.05 wt % for G = 5 and G = 30.

solar spectrum (solar simulator AM 1.5G), and the transmitted light was coupled to a spectrometer. Color rendering index (CRI) is an important measure that shows the ability to render true colors of the illuminated objects, and the transparent PDMS polymer matrix is a suitable material to be used for windows to keep the CRI of the transmitted light fixed in comparison with the incoming light generated by the solar simulator (Figure 3d). Remarkably, the InP/5ZnO QD-based LSC also exhibited no change in CRI with respect to the solar simulator, demonstrating its potential for solar windows (Table S3).

To investigate the effect of Stokes shift engineering on the LSC performance, the InP/2ZnO QDs with the highest QE and the InP/5ZnO QDs with the lowest reabsorption were integrated inside the PDMS waveguide (with the dimensions of 9 cm × 1.5 cm × 0.3 cm) at the same level of the weight percentage (0.05 wt %). We analyzed the dependence of the optical output power versus the illuminated area. For this, we covered a specific part of the LSCs, excited the remaining area with UV light (at 365 nm), and measured the optical output at the edge (Figure 4a inset). While the InP/2ZnO-based LSC had a near-exponential behavior, the InP/5ZnO-based LSC showed a linear response for the output optical power as the coverage area increased (Figure 4a). The linearity in InP/5ZnO LSC was due to the negligible reabsorption loss, whereas the reabsorption loss in InP/2ZnO LSC led to an exponential response while the illuminated area increased.

The emission spectra of InP/2ZnO and InP/5ZnO QD-LSCs were analyzed with the same configuration shown in the inset of Figure 4a under UV excitation. Even though the PL peak wavelength in the InP/2ZnO−polymer slab experienced a significant spectral peak shift (of $\Delta\lambda$ = 28.4 nm) at the end of the optical waveguide (Figure 4b), for the InP/5ZnO−polymer slab, the peak wavelength remained almost at the same value with a slight change (of $\Delta\lambda$ = 3.2 nm) because of the less overlap of the absorbance and PL spectra. Moreover, the spectral line width of the output intensity spectra is shown in Figure 4c, and the full width at half-maximum (fwhm) of the InP/5ZnO QD-LSC decreases with a lower slope (1.80 nm/cm) through the optical distance of 9 cm in comparison with the slope of the fwhm in InP/2ZnO QD-LSC (3.29 nm/cm) because of lower reabsorption. Figure 4d shows the PL decay through the LSC structure. However, because the reabsorption loss was low in InP/5ZnO QD-LSC, the scattering should have an effect on the observed decay. To evaluate the difference between scattering and reabsorption of QD-PDMS LSCs, a beam was propagated through PDMS and InP/5ZnO QD-LSC at the wavelength of 665 nm (Figure 4d inset).[17] The scattered light was collected from the upper face at different optical distances ranging from 1 to 8 cm from the excitation edge. As illustrated in Figure 4d, the scattering-corrected intensity, which was obtained by subtracting the optical output intensity of PDMS from that of the InP/5ZnO QD-LSC, nearly kept its intensity, and this demonstrated that the optical output decay was mainly due to scattering.

The optical efficiency is an important measure to evaluate the power conversion performance of LSCs. To measure the efficiency, we illuminated the surface of an LSC with a solar simulator and black-painted (blocked) all edges except one, which was coupled to the solar cell. We calculated the optical efficiency by using eq 1, where I_{LSC} is the short-circuit current of a solar cell coupled to the LSC when the LSC is illuminated by a solar simulator, A_{PV} is the area of the light collection edge, I_{PV} is the short-circuit current of a solar cell when the solar cell is directly illuminated by a solar simulator without an LSC, and A_{LSC} is the illumination area of the LSC surface.[15] The efficiency of InP/5ZnO QD-LSC with a geometrical factor of 5 corresponded to 1.45% at an optical transmission level of 73%.

$$\eta_{opt} = \frac{I_{LSC} \times A_{PV}}{I_{PV} \times A_{LSC}} \quad (1)$$

Moreover, we performed the analytical simulations to explore the highest possible optical efficiency by using eq 2,[6] in which $\langle\alpha_1\rangle$ is the averaged absorption coefficient of the QDs, d and L are the thickness and length of the LSC, respectively (Figure 5a), η_{PL} is the measured QE of the QDs in PDMS, η_{TIR} is the TIR efficiency for the PDMS polymer matrix, β is a numerical value fixed to 1.4 based on ref.,[53] and α_2 is the absorbance at the emission peak wavelength (see the Experimental Section for details). The results in Figure 5b showed that the optical efficiency of the LSCs can be controlled by varying the geometrical factor (G factor). We measured the optical efficiency of an LSC with a G factor of 30 as 0.24%, which was in agreement with the simulation in Figure 5b. Moreover, the efficiency levels can be improved over 20% by increasing the QE of the QDs over 60%. Further improvement in optical efficiency can be obtained by employing a back-reflector in the PV cells.

$$\eta_{opt} = \frac{1.05 \times (1 - R) \times (1 - e^{-\langle\alpha_1\rangle d})\eta_{PL}\eta_{TIR}}{1 + \beta\alpha_2 L(1 - \eta_{PL}\eta_{TIR})} \quad (2)$$

Downloaded from pubs.acs.org/aamick/article-pdf/10/15/12975/6692023/acsami.7b19144.pdf by KOC UNIV user on 29 October 2026

DOI: 10.1021/acsami.7b19144
ACS Appl. Mater. Interfaces 2018, 10, 12975−12982

The effect of the loading concentration on the optical efficiency was also investigated. Four different LSCs with different loading concentrations of 0.01, 0.05, 0.1, and 0.5 wt % of InP/5ZnO QDs were fabricated and illuminated with the solar spectrum. While the QE slightly decreased from 19.1% for 0.01 wt % to 16.4% for 0.5 wt %, the optical efficiency also increased from 0.28 to 3.22% (Figure S7 and Table 1). Here,

Table 1. Quantum Efficiency and Optical Efficiency of the Fabricated LSCs with Different Loading Concentrations of the InP/5ZnO Q Ds

	0.01 wt %	0.05 wt %	0.1 wt %	0.5 wt %
QE (%)	19.1	17.5	17.1	16.4
optical efficiency (%) $G = 30$	0.049	0.225	0.195	0.43
optical efficiency (%) $G = 5$	0.28	1.4	1.27	3.22

the optical efficiency is enhanced by increasing the loading concentration because of strong absorption (e.g., 0.5 wt %), but the transmission of the LSC significantly drops (e.g., to 13% at 525 nm) (Figure S8), which is not suitable for solar window applications. Therefore, it is important to optimize the light-harvesting and transmission properties of LSCs for solar window applications.

CONCLUSIONS

We demonstrated efficient LSCs based on cadmium-free QDs. The type-II band alignment of the InP/ZnO core/shell QDs enabled the Stokes shift engineering, which led to the suppression of the reabsorption losses. At the same time, the shell advantageously protected the recombination dynamics and QE against the host material effect. Indium-based optoelectronic materials and devices are already used in displays at homes and offices. Therefore, these indium phosphide nanomaterials may also find widespread use as LSCs in the windows.

EXPERIMENTAL SECTION

Chemicals. Zinc undecylenate (99%), OA (99%), OAM (99%), ODE (90%), indium (III) chloride ($InCl_3$) (99%), $P(TMS)_3$ (95%), and $Zn(acac)_2$ (99.995%) were purchased from Sigma-Aldrich. ODE was purified at 100 °C by evacuating and refilling repeatedly with nitrogen for 1 h. All the procedures were performed in a glovebox under a nitrogen atmosphere.

Indium Phosphide Core Synthesis. Zinc undecylenate (0.3 mmol), 98 μL of OA, and 204 μL of OAM were mixed in 9 mL of ODE in a 100 mL three-neck round-bottom flask. The solution was heated to 100 °C, evacuated, and refilled with nitrogen repeatedly to provide an oxygen- and water-free reaction atmosphere. $InCl_3$ (0.3 mmol) was then added to the solution in the glovebox. The flask was heated to 240 °C with strong agitation under nitrogen flow. At this temperature, 1.5 mL of phosphine stock solution ($P(TMS)_3$−ODE 0.2 mmol mL^{-1}) was injected to the solution swiftly. The color of the solution became dark right after the injection. The dark solution was kept at 210 °C for 20 min and then cooled down to room temperature.

Preparation of 0.015 M Zinc Oxide Stock Solution for the Shelling Process. $Zn(acac)_2$ (0.1 mmol), 32 μL of OA, and 1 mL of OAM were mixed in 6 mL of ODE at 60 °C.

InP/ZnO Quantum Dot Synthesis. The solution containing indium phosphide QDs was heated to 60 °C. Once the temperature was stable, 530 μL of the prepared zinc oxide stock solution was added to the indium phosphide solution. Then, the solution was heated up to 280 °C and stirred for 20 min.

Indium Phosphide Quantum Dots with Multiple Shelling of Zinc Oxide. For the preparation of the InP/2ZnO, InP/3ZnO, InP/4ZnO, and InP/5ZnO QDs, 670, 835, 1170, and 1835 μL of the prepared zinc oxide stock solution were added, respectively. The rest of the shelling process was the same as that of the InP/ZnO procedure.

Purification and Storage. Four milliliters of toluene were added to the QD solution, and the precipitate was centrifuged at 9000 rpm for 15 min and removed. Ethanol was added to the solution until it became turbid, and then the solution was centrifuged at 9000 rpm for 5 min three times. The precipitated QDs were dispersed in hexane or toluene. The purified QD solutions were kept at 5 °C.

Device Fabrication. Six milligrams of purified QDs was dissolved in 1 mL hexane solvent as the stock solution. For the preparation of each slab, 355 μL of the QD stock solution, 4.5 mL of PDMS Sylgard 184, and 0.45 mL of Sylgard 184 curing agent were used. The mixture was degassed repeatedly and kept under vacuum for 20 min. Figure S5 represents the dimensions of the fabricated aluminum mold, and the degassed mixture was transferred to the mold and cured at 70 °C for 6 h. The cured LSC was peeled off from the aluminum mold after the completion of the heating process.

Methods and Characterization. PXRD measurements of QDs were carried out by a Bruker D2 PHASER X-ray diffractometer [$\lambda_{Cu\ K\alpha}$ = 1.54 Å] with a scan rate of 1° min^{-1}. To prepare samples for XRD measurements, we purified the synthesized QDs three times to remove excess impurities (including excess zinc precursor). Then, we drop-casted the QD solution dispersed in hexane on a silicon holder and then heated up to 100 °C for 2 h to ensure the evaporation of organics. The powder samples were supported by the poly(methyl methacrylate) holder, and the studies were carried out at room temperature. The UV/visible absorption and PL spectra of QDs were carried out by an Edinburgh Instruments spectrofluorometer FS5. The system included a 150 W xenon lamp combined with an excitation monochromator. The excitation source was set to 375 nm with a band-pass filter that has an fwhm of 2 nm. The QDs in hexane are poured into standard quartz cuvettes for absorbance and PL. The emission detector was a single-photon-counting photomultiplier tube (R928P), and the detection spectral width was 2 nm. Absolute fluorescence QE values were measured by using an integrating sphere. The measurement module that contained an integrating sphere with an inner diameter of 150 mm was placed into the FS5 system for the determination of QE. Time-resolved microscopy was carried out by a PicoQuant MicroTime 100 time-resolved fluorescence microscope. A PDL 800-D diode laser driver for picosecond pulses combined with a 375 nm laser head was used as the excitation source with a repetition rate of 8 MHz. A single-photon-sensitive detector (PMA Hybrid 50) based on a photomultiplier tube (R10467 from Hamamatsu) was used. The time-correlated single-photon-counting electronics of HydraHarp 400 was adjusted to a resolution of 4 ps. The samples were measured at room temperature. The SEM−EDXS measurements were obtained by a Zeiss Ultra Plus field emission scanning electron microscope by using a Bruker XFlash 5010 EDXS detector. The accelerating voltage was set to 20 kV. The samples were prepared by drying the QDs dissolved in the hexane solution to 300 °C for 1 h. TEM imaging was performed using a 200 keV accelerating voltage in a spherical aberration-corrected scanning TEM (JEOL JEM-200ARMCF). Diffraction contrast images, for estimating the particle size distribution, were recorded using a 60 μm objective aperture. Phase-contrast, high-resolution TEM imaging was performed for investigating crystallinity in the specimen. Z-contrast imaging was performed using a collection semiangle range of 53.4−214 mrad and a probe size of ca. 2 Å.

For optical efficiency measurements, a calibrated Newport Oriel LCS-100 solar simulator AM 1.5G was used. The output power of the Xe lamp was 100 mW/cm^2. A silicon solar cell with the dimensions of 110 mm × 70 mm was used. Because the surface area of the solar cell was greater than the LSC's edge area (1.5 cm × 0.3 cm), a black tape was used to mask the excessive area. For measuring R, eq 3 was used.

$$R = \frac{(n_{PDMS} - n_{air})^2}{(n_{PDMS} + n_{air})^2} \quad (3)$$

By considering n_{PDMS} = 1.4,[54] the reflectance yielded was 0.027. The averaged absorption coefficient ($\langle\alpha_1\rangle$) can be calculated based on eq 4.

Downloaded from pubs.acs.org/aamick/article-pdf/10/15/12975/6692023/acsami.7b19144.pdf by KOC UNIV user on 29 October 2026

DOI: 10.1021/acsami.7b19144
ACS Appl. Mater. Interfaces 2018, 10, 12975−12982

$$\langle \alpha_1 \rangle = -\frac{1}{d} \ln\left(\frac{\int_{\lambda_1}^{\infty} S_{in}(\lambda)\, e^{-\alpha(\lambda)d}\, d(\lambda)}{\int_{\lambda_1}^{\infty} S_{in}(\lambda)\, d(\lambda)} \right) \quad (4)$$

in which λ_1 is the wavelength at which the QDs start to absorb light.[6] $\langle \alpha_1 \rangle$ was calculated as 0.0585. Moreover, η_{TIR} was calculated as 0.85, and based on the emission and absorption spectra, α_2 was calculated as 0.001. For the preparation of an LSC with a gain factor of 5, an InP/5ZnO QD-LSC was fabricated with the dimensions of 1.5 cm × 1.5 cm × 0.3 cm at a QD weight percentage of 0.05.

■ ASSOCIATED CONTENT

Supporting Information

The Supporting Information is available free of charge on the ACS Publications website at DOI: 10.1021/acsami.7b19144.

TEM images of the QDs, ML coverage calculation, XRD and SEM−EDXS measurements, preparation of LSCs, Fourier transform infrared measurement, and optical properties of the LSCs with different loading concentrations (PDF)

■ AUTHOR INFORMATION

Corresponding Author

*E-mail: snizamoglu@ku.edu.tr.

ORCID

Sadra Sadeghi: 0000-0002-8569-1626
Houman Bahmani Jalali: 0000-0001-7212-9098
Rustamzhon Melikov: 0000-0003-2214-7604
Baskaran Ganesh Kumar: 0000-0003-4705-499X
Cleva W. Ow-Yang: 0000-0002-2909-0957
Sedat Nizamoglu: 0000-0003-0394-5790

Author Contributions

⊥S.S. and H.B.J. contributed equally to the paper.

Notes

The authors declare no competing financial interest.

■ ACKNOWLEDGMENTS

S.N. acknowledges the support by the European Research Council (ERC) under the European Union's Horizon 2020 Research and Innovation Programme (grant agreement no. 639846). The authors acknowledge Dr. Ceren Yilmaz Akkaya for XRD and Dr. Baris Yagci for SEM−EDXS measurements at KUYTAM (Koç University Surface Science and Technology Center). The authors gratefully acknowledge Prof. Funda Yagci Acar for fluorescence spectroscopy measurements and Prof. Ismail Lazoglu and Muzaffer Butun for their support on fabrication of the LSC mold. The authors also thank Prof. Mehmet Sahin at Abdullah Gul University for scientific discussion on the electronic properties of QDs.

■ REFERENCES

(1) Coropceanu, I.; Bawendi, M. G. Core/shell Quantum Dot Based Luminescent Solar Concentrators with Reduced Reabsorption and Enhanced Efficiency. *Nano Lett.* **2014**, *14*, 4097−4101.

(2) Debije, M. G.; Verbunt, P. P. C. Thirty Years of Luminescent Solar Concentrator Research: Solar Energy for the Built Environment. *Adv. Energy Mater.* **2012**, *2*, 12−35.

(3) van Sark, W. G. J. H. M.; Barnham, K. W. J.; Slooff, L. H.; Chatten, A. J.; Büchtemann, A.; Meyer, A.; McCormack, S. J.; Koole, R.; Farrell, D. J.; Bose, R. Luminescent Solar Concentrators—A Review of Recent Results. *Opt. Express* **2008**, *16*, 21773−21792.

(4) Yoon, J.; Li, L.; Semichaevsky, A. V.; Ryu, J. H.; Johnson, H. T.; Nuzzo, R. G.; Rogers, J. A. Flexible Concentrator Photovoltaics Based on Microscale Silicon Solar Cells Embedded in Luminescent Waveguides. *Nat. Commun.* **2011**, *2*, 343.

(5) Fraunhofer, I.; Energiewende, A. Current and Future Cost of Photovoltaics; Long-term Scenarios for Market Development, System Prices and LCOE of Utilityscale PV-systems. *Agora Energiewende*; Fraunhofer ISE, 2015; p 82.

(6) Zhao, H.; Zhou, Y.; Benetti, D.; Ma, D.; Rosei, F. Perovskite Quantum Dots Integrated in Large-area Luminescent Solar Concentrators. *Nano Energy* **2017**, *37*, 214−223.

(7) Sharma, M.; Gungor, K.; Yeltik, A.; Olutas, M.; Guzelturk, B.; Kelestemur, Y.; Erdem, T.; Delikanli, S.; McBride, J. R.; Demir, H. V. Near-Unity Emitting Copper-Doped Colloidal Semiconductor Quantum Wells for Luminescent Solar Concentrators. *Adv. Mater.* **2017**, *29*, 1700821.

(8) Chatten, A. J.; Barnham, K. W. J.; Buxton, B. F.; Ekins-Daukes, N. J.; Malik, M. A. Quantum Dot Solar Concentrators. *Semiconductors* **2004**, *38*, 909−917.

(9) Currie, M. J.; Mapel, J. K.; Heidel, T. D.; Goffri, S.; Baldo, M. A. High-efficiency Organic Solar Concentrators for Photovoltaics. *Science* **2008**, *321*, 226−228.

(10) Bellina, F.; Manzini, C.; Marianetti, G.; Pezzetta, C.; Fanizza, E.; Lessi, M.; Minei, P.; Barone, V.; Pucci, A. Colourless p-phenylene-spaced bis-azoles for Luminescent Concentrators. *Dyes Pigm.* **2016**, *134*, 118−128.

(11) Li, H.; Wu, K.; Lim, J.; Song, H.-J.; Klimov, V. I. Doctor-blade Deposition of Quantum Dots onto Standard Window Glass for Low-loss Large-area Luminescent Solar Concentrators. *Nat. Energy* **2016**, *1*, 16157.

(12) Aeberhard, U.; Vaxenburg, R.; Lifshitz, E.; Tomić, S. Fluorescence of Colloidal PbSe/PbS QDs in NIR Luminescent Solar Concentrators. *Phys. Chem. Chem. Phys.* **2012**, *14*, 16223−16228.

(13) Weber, W. H.; Lambe, J. Luminescent Greenhouse Collector for Solar Radiation. *Appl. Opt.* **1976**, *15*, 2299−2300.

(14) Goetzberger, A.; Greube, W. Solar Energy Conversion with Fluorescent Collectors. *Appl. Phys. A: Mater. Sci. Process.* **1977**, *14*, 123−139.

(15) Nikolaidou, K.; Sarang, S.; Hoffman, C.; Mendewala, B.; Ishihara, H.; Lu, J. Q.; Ilan, B.; Tung, V.; Ghosh, S. Hybrid Perovskite Thin Films as Highly Efficient Luminescent Solar Concentrators. *Adv. Opt. Mater.* **2016**, *4*, 2126−2132.

(16) Jin, L.; Sirigu, G.; Tong, X.; Camellini, A.; Parisini, A.; Nicotra, G.; Spinella, C.; Zhao, H.; Sun, S.; Morandi, V. Engineering Interfacial Structure in "Giant" PbS/CdS Quantum Dots for Photoelectrochemical Solar Energy Conversion. *Nano Energy* **2016**, *30*, 531−541.

(17) Meinardi, F.; Colombo, A.; Velizhanin, K. A.; Simonutti, R.; Lorenzon, M.; Beverina, L.; Viswanatha, R.; Klimov, V. I.; Brovelli, S. Large-area Luminescent Solar Concentrators Based on "Stokes-shift-engineered" nanocrystals in a Mass-polymerized PMMA Matrix. *Nat. Photonics* **2014**, *8*, 392−399.

(18) Chemisana, D. Building Integrated Concentrating Photovoltaics: a Review. *Renewable Sustainable Energy Rev.* **2011**, *15*, 603−611.

(19) Nizamoglu, S.; Mutlugun, E.; Özel, T.; Demir, H. V.; Sapra, S.; Gaponik, N.; Eychmüller, A. Dual-color Emitting Quantum-dot-quantum-well CdSe-ZnS Heteronanocrystals Hybridized on InGaN/GaN Light Emitting Diodes for High-quality White Light Generation. *Appl. Phys. Lett.* **2008**, *92*, 113110.

(20) Gaponenko, S. V. *Optical Properties of Semiconductor Nanocrystals*; Cambridge University Press, 1998; Vol. *23*.

(21) Chatten, A. J.; Barnham, K. W. J.; Buxton, B. F.; Ekins-Daukes, N. J.; Malik, M. A. Quantum Dot Solar Concentrators. *Semiconductors* **2004**, *38*, 909−917.

(22) Krumer, Z.; Pera, S. J.; van Dijk-Moes, R. J. A.; Zhao, Y.; de Brouwer, A. F. P.; Groeneveld, E.; van Sark, W. G. J. H. M.; Schropp, R. E. I.; de Mello Donegá, C. Tackling Self-absorption in Luminescent Solar Concentrators with Type-II Colloidal Quantum Dots. *Sol. Energy Mater. Sol. Cells* **2013**, *111*, 57−65.

Downloaded from pubs.acs.org/aamick/article-pdf/10/15/12975/6692023/acsami.7b19144.pdf by KOC UNIV user on 29 October 2026

DOI: 10.1021/acsami.7b19144
ACS Appl. Mater. Interfaces 2018, 10, 12975−12982

(23) Erickson, C. S.; Bradshaw, L. R.; McDowall, S.; Gilbertson, J. D.; Gamelin, D. R.; Patrick, D. L. Zero-Reabsorption Doped-nanocrystal Luminescent Solar Concentrators. *ACS Nano* **2014**, *8*, 3461−3467.
(24) Meinardi, F.; McDaniel, H.; Carulli, F.; Colombo, A.; Velizhanin, K. A.; Makarov, N. S.; Simonutti, R.; Klimov, V. I.; Brovelli, S. Highly Efficient Large-area Colourless Luminescent Solar Concentrators Using Heavy-metal-free Colloidal Quantum Dots. *Nat. Nanotechnol.* **2015**, *10*, 878−885.
(25) Zhao, H.; Vomiero, A.; Rosei, F. Ultrasensitive, Biocompatible, Self-Calibrating, Multiparametric Temperature Sensors. *Small* **2015**, *11*, 5741−5746.
(26) Zhao, H.; Benetti, D.; Jin, L.; Zhou, Y.; Rosei, F.; Vomiero, A. Absorption Enhancement in "Giant" Core/Alloyed-Shell Quantum Dots for Luminescent Solar Concentrator. *Small* **2016**, *12*, 5354−5365.
(27) Zhao, H.; Sirigu, G.; Parisini, A.; Camellini, A.; Nicotra, G.; Rosei, F.; Morandi, V.; Zavelani-Rossi, M.; Vomiero, A. Dual Emission in Asymmetric "Giant" PbS/CdS/CdS Core/Shell/Shell Quantum Dots. *Nanoscale* **2016**, *8*, 4217−4226.
(28) Debije, M. G. Solar Energy Collectors with Tunable Transmission. *Adv. Funct. Mater.* **2010**, *20*, 1498−1502.
(29) Desmet, L.; Ras, A. J. M.; de Boer, D. K. G.; Debije, M. G. Monocrystalline Silicon Photovoltaic Luminescent Solar Concentrator with 4.2% Power Conversion Efficiency. *Opt. Lett.* **2012**, *37*, 3087−3089.
(30) Wang, Z.; Yang, W.; Wang, Y. Self-Trapped Exciton and Large Stokes Shift in Pristine and Carbon-Coated Silicon Carbide Quantum Dots. *J. Phys. Chem. C* **2017**, *121*, 20031−20038.
(31) Bailey, R. E.; Nie, S. Alloyed Semiconductor Quantum Dots: Tuning the Optical Properties without Changing the Particle Size. *J. Am. Chem. Soc.* **2003**, *125*, 7100−7106.
(32) Bryan, J. D.; Gamelin, D. R. Doped Semiconductor Nanocrystals: Synthesis, Characterization, Physical Properties, and Applications. *Progress in Inorganic Chemistry*; John Wiley & Sons, Inc., 2005; Vol. *54*, pp 47−126.
(33) Viswanatha, R.; Brovelli, S.; Pandey, A.; Crooker, S. A.; Klimov, V. I. Copper-doped Inverted Core/Shell Nanocrystals with "Permanent" Optically Active Holes. *Nano Lett.* **2011**, *11*, 4753−4758.
(34) Sahu, A.; Kang, M. S.; Kompch, A.; Notthoff, C.; Wills, A. W.; Deng, D.; Winterer, M.; Frisbie, C. D.; Norris, D. J. Electronic Impurity Doping in CdSe Nanocrystals. *Nano Lett.* **2012**, *12*, 2587−2594.
(35) Hutton, M. Human Health Concerns of Lead, Mercury, Cadmium and Arsenic. *Lead, Mercury, Cadmium and Arsenic in the Environment*; John Wiley & Sons Ltd, 1987; Vol. *31*, pp 53−68.
(36) Baker, J. New Technology and Possible Advances in Energy Storage. *Energy Policy* **2008**, *36*, 4368−4373.
(37) Chan, W. C. W.; Nie, S. Quantum Dot Bioconjugates for Ultrasensitive Nonisotopic Detection. *Science* **1998**, *281*, 2016−2018.
(38) Clapp, A. R.; Medintz, I. L.; Mauro, J. M.; Fisher, B. R.; Bawendi, M. G.; Mattoussi, H. Fluorescence Resonance Energy Transfer Between Quantum Dot Donors and Dye-labeled Protein Acceptors. *J. Am. Chem. Soc.* **2004**, *126*, 301−310.
(39) Michalet, X.; Pinaud, F. F.; Bentolila, L. A.; Tsay, J. M.; Doose, S.; Li, J. J.; Sundaresan, G.; Wu, A. M.; Gambhir, S. S.; Weiss, S. Quantum Dots for Live Cells, In Vivo Imaging, and Diagnostics. *Science* **2005**, *307*, 538−544.
(40) Mutlugun, E.; Hernandez-Martinez, P. L.; Eroglu, C.; Coskun, Y.; Erdem, T.; Sharma, V. K.; Unal, E.; Panda, S. K.; Hickey, S. G.; Gaponik, N. Large-area (over 50 cm × 50 cm) Freestanding Films of Colloidal InP/ZnS Quantum Dots. *Nano Lett.* **2012**, *12*, 3986−3993.
(41) Pust, P.; Schmidt, P. J.; Schnick, W. A Revolution in Lighting. *Nat. Mater.* **2015**, *14*, 454−458.
(42) Van de Walle, C. G.; Neugebauer, J. Universal Alignment of Hydrogen Levels in Semiconductors, Insulators and Solutions. *Nature* **2003**, *423*, 626−628.
(43) Du, Y.-P.; Zhang, Y.-W.; Sun, L.-D.; Yan, C.-H. Efficient Energy Transfer in Monodisperse Eu-doped ZnO Nanocrystals Synthesized from Metal Acetylacetonates in High-boiling Solvents. *J. Phys. Chem. C* **2008**, *112*, 12234−12241.
(44) Salavati-Niasari, M.; Davar, F.; Mazaheri, M. Preparation of ZnO Nanoparticles from [bis(acetylacetonato)zinc(II)]−oleylamine Complex by Thermal Decomposition. *Mater. Lett.* **2008**, *62*, 1890−1892.
(45) Liu, J. F.; Bei, Y. Y.; Wu, H. P.; Shen, D.; Gong, J. Z.; Li, X. Y.; Wang, Y. W.; Jiang, N. P.; Jiang, J. Z. Synthesis of Relatively Monodisperse ZnO Nanocrystals from a Precursor zinc 2,4-pentanedionate. *Mater. Lett.* **2007**, *61*, 2837−2840.
(46) Musić, S.; Šarić, A.; Popović, S. Formation of Nanosize ZnO Particles by Thermal Decomposition of zinc acetylacetonate Monohydrate. *Ceram. Int.* **2010**, *36*, 1117−1123.
(47) Nguyen, T.-L.; Michael, M.; Mulvaney, P. Synthesis of Highly Crystalline CdSe@ ZnO Nanocrystals via Monolayer-by-monolayer Epitaxial Shell Deposition. *Chem. Mater.* **2014**, *26*, 4274−4279.
(48) Xu, S.; Ziegler, J.; Nann, T. Rapid Synthesis of Highly Luminescent InP and InP/ZnS Nanocrystals. *J. Mater. Chem.* **2008**, *18*, 2653−2656.
(49) Ramasamy, P.; Kim, B.; Lee, M.-S.; Lee, J.-S. Beneficial Effects of Water in the Colloidal Synthesis of InP/ZnS Core−shell Quantum Dots for Optoelectronic Applications. *Nanoscale* **2016**, *8*, 17159−17168.
(50) Smith, A. M.; Mohs, A. M.; Nie, S. Tuning the Optical and Electronic Properties of Colloidal Nanocrystals by Lattice Strain. *Nat. Nanotechnol.* **2009**, *4*, 56−63.
(51) Manjceevan, A.; Bandara, J. Robust Surface Passivation of Trap Sites in PbS q-dots by Controlling the Thickness of CdS Layers in PbS/CdS Quantum Dot Solar Cells. *Sol. Energy Mater. Sol. Cells* **2016**, *147*, 157−163.
(52) Dabbousi, B. O.; Rodriguez-Viejo, J.; Mikulec, F. V.; Heine, J. R.; Mattoussi, H.; Ober, R.; Jensen, K. F.; Bawendi, M. G. (CdSe)ZnS Core−shell Quantum Dots: Synthesis and Characterization of a Size Series of Highly Luminescent Nanocrystallites. *J. Phys. Chem. B* **1997**, *101*, 9463−9475.
(53) Klimov, V. I.; Baker, T. A.; Lim, J.; Velizhanin, K. A.; McDaniel, H. Quality Factor of Luminescent Solar Concentrators and Practical Concentration Limits Attainable with Semiconductor Quantum Dots. *ACS Photonics* **2016**, *3*, 1138−1148.
(54) Chang-Yen, D. A.; Eich, R. K.; Gale, B. K. A Monolithic PDMS Waveguide System Fabricated Using Soft-lithography Techniques. *J. Lightwave Technol.* **2005**, *23*, 2088.

Downloaded from pubs.acs.org/aamick/article-pdf/10/15/12975/6692023/acsami.7b19144.pdf by KOC UNIV user on 29 October 2026

DOI: 10.1021/acsami.7b19144
ACS Appl. Mater. Interfaces 2018, 10, 12975−12982